SPARTA – Solver for Polarized Atmospheric Radiative Transfer Applications: Introduction and application to Saharan dust fields

Vasileios Barlakas [a,b,*], Andreas Macke [b], Manfred Wendisch [a]

[a] Leipzig Institute for Meteorology, University of Leipzig, Stephanstr. 3, Leipzig, Germany
[b] Leibniz Institute for Tropospheric Research, Permoserstr. 15, Leipzig, Germany

ARTICLE INFO

ABSTRACT

Non-spherical particles in the atmosphere absorb and scatter solar radiation. They change the polarization state of solar radiation depending on their shape, size, chemical composition and orientation. To quantify polarization effects, a new three-dimensional (3D) vector radiative transfer model, SPARTA (Solver for Polarized Atmospheric Radiative Transfer Applications) is introduced and validated against benchmark results. SPARTA employs the statistical forward Monte Carlo technique for efficient column-response pixel-based radiance calculations including polarization for 3D inhomogeneous cloudless and cloudy atmospheres. A sensitivity study has been carried out and exemplarily results are presented for two lidar-based mineral dust fields. The scattering and absorption properties of the dust particles have been computed for spheroids and irregular shaped particles. Polarized radiance fields in two-dimensional (2D) and one-dimensional (1D) inhomogeneous Saharan dust fields have been calculated at 532 nm wavelength. The domain-averaged results of the normalized reflected radiance are almost identical for the 1D and 2D modes. In the areas with large spatial gradient in optical thickness with expected significant horizontal photon transport, the radiance fields of the 2D mode differ by about $\pm 12\%$ for the first Stokes component (radiance, I) and $\pm 8\%$ for the second Stokes component (linear polarization, Q) from the fields of the 1D mode.

1. Introduction

Non-spherical atmospheric mineral dust particles are known to have a considerable impact on climate [37,33,29]. However, these particles yet have not been assigned a reliable assessment of their impact, partly owing to incomplete understanding of their properties [29]. They scatter, absorb and polarize solar radiation depending on their shape, size, chemical composition and orientation. These processes are rather complex, but their knowledge is important for the interpretation of remote-sensing measurements. Moreover, the use of polarization measurements is sensitive to particle microphysical properties and could ameliorate such problems (e.g. [25,44,6,36]). Nowadays, several remote sensing instruments employ polarization. For example, the POLarization and Directionality of the Earth's Reflectances (POLDER) instrument included polarized information [19], the Research Scanning Polarimeter (RPS) [11,10], the Multiangle SpectroPolarimetric Imager [21], and the CIMEL polarized sun/sky-photometer developed by CIMEL Electronique (Paris, France) CE318-DP [35] were developed for polarization measurements.

The investigation of ground-based and airborne passive radiance and polarization measurements necessitates radiative transfer models that accounts for multiple scattering, absorption, and polarization. As a result, a growing number of 1D and 3D vector models have been developed [22]. In most cases, the 1D polarized radiative transfer models are freely available. The 3D radiative transfer simulations demand high computational power. Furthermore, during the last decades, there has been an inconclusive debate about whether the 1D approximation is sufficient or the neglect of horizontal photon transport causes significant errors in radiance simulations [20].

Although there has been only limited research on the radiative effects due to horizontal photon transport for dust fields [56], several studies have been carried out for inhomogeneous liquid water, mixed phase and ice clouds (e.g., [16,52,53,4,20,9]). However, in these studies the issue under scrutiny is the radiative effects in the scalar radiative transfer scheme. In this paper, the discussion centers on polarization effects.

A new vector model based on the forward Monte Carlo method is introduced. It simulates 3D radiative transfer processes in arbitrary complex scattering and absorbing media. Validations of SPARTA against benchmark results are also presented. Polarization radiative effects for lidar-measured inhomogeneous Saharan dust fields are discussed, performing 2D and 1D reflectance calculations using SPARTA.

2. Radiative transfer solver SPARTA

The Solver for Polarized Atmospheric Radiative Transfer Applications (SPARTA) is a new 3D vector radiative transfer model. A preliminary version of SPARTA was discussed in Barlakas et al. [3]. The model employs the forward Monte Carlo technique and computes column-response pixel-based radiances for 3D inhomogeneous cloudless and cloudy atmospheres. It is based on the scalar Monte Carlo model of the UNIversity of Kiel (MC-UNIK, [40]), which participated in the international Intercomparison of 3D Radiation Codes (I3RC, [9]). MC-UNIK has been extended to account for polarization effects due to multiple scattering by non-spherical particles, i.e., coarse mode dust or ice particles. The details of the implementation of polarization in MC-UNIK are presented in this paper; the differences between MC-UNIK and SPARTA are outlined.

The conventional approach to consider polarization dates back to Stokes [54], who discovered that the polarization behavior of the electromagnetic radiation could be represented by real observables. This resulted in the Stokes vector, defined by four components:

$$\vec{\mathbf{S}} = \begin{pmatrix} I \\ Q \\ U \\ V \end{pmatrix}, \tag{1}$$

each of them carrying the units of irradiance (W m^{-2}) [54].

The Stokes vector is described by the components of a transverse electromagnetic field [13,25,28,38,45,60]:

$$I = \frac{1}{2}\sqrt{\frac{\epsilon}{\kappa}} \cdot (E_l \cdot E_l^* + E_r \cdot E_r^*), \tag{2}$$

$$Q = \frac{1}{2}\sqrt{\frac{\epsilon}{\kappa}} \cdot (E_l \cdot E_r^* - E_r \cdot E_r^*), \tag{3}$$

$$U = \frac{1}{2}\sqrt{\frac{\epsilon}{\kappa}} \cdot (E_l \cdot E_r^* + E_r \cdot E_l^*), \tag{4}$$

$$V = i \cdot \frac{1}{2}\sqrt{\frac{\epsilon}{\kappa}} \cdot (E_l \cdot E_r^* - E_r \cdot E_l^*). \tag{5}$$

where E_l and E_r are the two orthogonal components of the harmonic electromagnetic field vector parallel (subscript "l") and perpendicular (subscript "r") to the direction of propagation. ϵ is the electric permittivity, κ is the magnetic permeability. The asterisk stands for the complex conjugate value, and $i = \sqrt{-1}$. The first Stokes vector element, I, represents the total irradiance, Q and U describe the linear and V the circular polarization. These parameters are defined such that the local meridional plane represents the plane of reference [13], defined by the photon (i.e. incident or scattering) and vertical directions.

SPARTA considers a 3D Cartesian cuboidal domain, in which individual photons are traced throughout their propagation. In Monte Carlo theory, photons refer to imaginary discrete "packets" or "units" of the incident energy rather than the physical photons (quantum electrodynamics) [43]. The 3D domain is split into grid-boxes, defined by geometrical dimensions along x-, y-, and z-directions, a total volumetric scattering β_{sca}^{tot} and extinction coefficients β_{ext}^{tot}, a total scattering phase matrix $\mathbf{P}^{tot}(\Theta)$ with the scattering angle Θ, and a total single scattering albedo ω_0^{tot}. The superscript "tot" indicates the combined optical properties of the different types of particles (e.g., molecules, aerosol particles, and cloud particles), which are contained in each grid-box. A 2D representation of the model domain is illustrated in Fig. 1.

Photon propagation is defined by the azimuth and zenith angles [12]. The azimuth angle φ is measured clockwise when looking upwards and the zenith angle θ is the angle with respect to the upward normal direction. Accordingly, the initial incident direction (subscript "inc") is expressed in terms of the solar position with a direction derived from the directional cosines:

$$\widehat{k}_{inc,0} = \begin{pmatrix} k_{inc,0}^x \\ k_{inc,0}^y \\ k_{inc,0}^z \end{pmatrix} = \begin{pmatrix} \sin\theta_0 \cdot \cos\varphi_0 \\ \sin\theta_0 \cdot \sin\varphi_0 \\ -\cos\theta_0 \end{pmatrix}, \tag{6}$$

where θ_0 and φ_0 are the solar zenith and azimuth angles, respectively.

In the vector scheme, the incident quasi-monochromatic electromagnetic wave is considered unpolarized and characterized by a weight, the Stokes weight, whose value is set originally to unity, $\vec{\mathbf{S}}_{inc} = (1\ 0\ 0\ 0)^T$ (superscript "T" represents the transpose vector).

In the Monte Carlo technique the propagation of photons through a medium is traced. Following Marchuk et al.
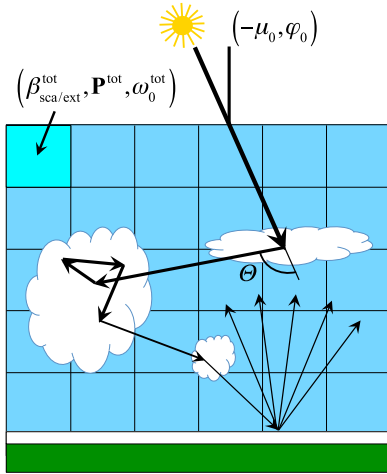
Fig. 1. 2D representation of the scheme of the photon path within the 3D domain of the Monte Carlo radiative transfer model: $(-\mu_0, \varphi_0)$ is the initial incident photon direction defined by the cosine of the solar zenith ($\mu_0 = \cos\theta_0$) and azimuth angles (φ_0), $\beta_{\text{sca/ext}}^{\text{tot}}$ stands for either the total volumetric scattering (subscript "sca") or extinction coefficients (subscript "ext"), $\mathbf{P}^{\text{tot}}$ for the total scattering phase matrix, and ω_0^{tot} is the total single scattering albedo. The superscript "tot" indicates the combined optical properties of the different types of particles, which are contained in each grid-box.

[41], the free path lengths of a photon are simulated by random number processes with attenuation described by the law of Bouguer–Beer. In the original MC-UNIK model, the later procedure corresponds to the probability density function:

$$p_{\text{ext}} = \exp\left(-\int_0^l \beta_{\text{ext}}^{\text{tot}}\, \mathrm{d}l\right). \tag{7}$$

$\beta_{\text{ext}}^{\text{tot}}$ is the total volumetric extinction coefficient and $\mathrm{d}l$ is the path element of the photon path. Consequently, at each scattering event, absorption is considered by reducing the original scalar weight by multiplication with the single scattering albedo. However, in SPARTA, the free path length is determined by the total volumetric scattering coefficient ($\beta_{\text{sca}}^{\text{tot}}$) and the probability density function is given by:

$$p_{\text{sca}} = \exp\left(-\int_0^l \beta_{\text{sca}}^{\text{tot}}\, \mathrm{d}l\right). \tag{8}$$

Absorption is taken into account by decreasing the initial Stokes weight by the estimated total absorption coefficient ($\beta_{\text{abs}}^{\text{tot}}$), along the photon path, with the Bouguer–Beer law:

$$p_{\text{abs}} = \exp\left(-\int_0^l \beta_{\text{abs}}^{\text{tot}}\, \mathrm{d}l\right). \tag{9}$$

A major difference between the scalar and the vector approaches involves amendments in the scattering description. In case of a scattering event, the new propagation direction (scattering direction, subscript "sca") needs to be calculated $\widehat{k}_{\text{sca}}$ from the previous direction ($\widehat{k}_{\text{inc}}$ or $\widehat{k}_{\text{inc,0}}$ in case of the first scattering event) and the scattering zenith and azimuth angles [41]. For scalar radiative transfer theory, the scalar phase function P,

representing the relative angular distribution of the scattered radiation [60], is adequate to describe the scattering behavior. It depends only on the scattering angle with respect to the incident direction, omitting any azimuthal angular dependence. Polarization introduces an anisotropy of the scattering direction depending on the frame of reference. Consequently, the interaction between a photon and a particle is described by a 4×4 matrix, the scattering phase matrix $\mathbf{P}$. Considering an ensemble of randomly oriented particles that form a macroscopically isotropic and mirror-symmetric scattering medium, the number of scattering phase matrix elements is reduced to six [28]:

$$\mathbf{P}(\Theta) = \begin{pmatrix} P_{11}(\Theta) & P_{12}(\Theta) & 0 & 0 \\ P_{12}(\Theta) & P_{22}(\Theta) & 0 & 0 \\ 0 & 0 & P_{33}(\Theta) & P_{34}(\Theta) \\ 0 & 0 & -P_{34}(\Theta) & P_{44}(\Theta) \end{pmatrix}. \tag{10}$$

The scattering phase matrix is defined with respect to the scattering plane, defined by the incident and the scattering directions. Furthermore, it relates the Stokes vector elements linked to the two directions, specified with respect to their reference planes [45]. In order to derive the Stokes vector of the scattered electromagnetic wave $\vec{\mathbf{S}}_{\text{sca}}$ with respect to its plane of reference (plane containing the scattering and the vertical directions) the incident Stokes vector has to be transformed to the scattering plane so that the scattering phase matrix multiplication can be carried out. The scattered Stokes vector is given by:

$$\vec{\mathbf{S}}_{\text{sca}} = \mathbf{R}(-\eta_2) \cdot \mathbf{P}(\Theta) \cdot \mathbf{R}(\pi - \eta_1) \cdot$$
$$\vec{\mathbf{S}}_{\text{inc}} = \mathbf{Z}(\theta_{\text{inc}}, \varphi_{\text{inc}}; \theta_{\text{sca}}, \varphi_{\text{sca}}). \tag{11}$$

Here $\mathbf{Z}$ is the transformation phase matrix that describes the scattering procedure, η_1 and η_2 are the rotation angles, and $\mathbf{R}(\eta)$ is the rotation matrix (see Fig. 2):

$$\mathbf{R}(\eta) = \begin{pmatrix} 1 & 0 & 0 & 0 \\ 0 & \cos 2\eta & -\sin 2\eta & 0 \\ 0 & \sin 2\eta & \cos 2\eta & 0 \\ 0 & 0 & 0 & 1 \end{pmatrix}. \tag{12}$$

The rotation angles are computed from $\widehat{k}_{\text{inc}}$ and $\widehat{k}_{\text{sca}}$ using spherical trigonometry [45]:

$$\cos \eta_1 = \frac{\cos \theta_{\text{sca}} - \cos \theta_{\text{inc}} \cdot \cos \Theta}{\sin \theta_{\text{inc}} \cdot \sin \Theta}, \tag{13}$$

$$\cos \eta_2 = \frac{\cos \theta_{\text{inc}} - \cos \theta_{\text{sca}} \cdot \cos \Theta}{\sin \theta_{\text{sca}} \cdot \sin \Theta}. \tag{14}$$

The following relations are additionally used:

$$\cos 2\eta = 2 \cdot \cos^2 \eta - 1, \tag{15}$$

$$\sin 2\eta = \pm 2 \cdot \sqrt{(1 - \cos^2 \eta)} \cdot \cos \eta, \tag{16}$$

where η represents both η_1 or η_2. The sign depends on the difference $(\varphi_{\text{sca}} - \varphi_{\text{inc}})$. When $0 \leq (\varphi_{\text{sca}} - \varphi_{\text{inc}}) \leq \pi$, one should use the "+" sign. When $0 \leq (\varphi_{\text{inc}} - \varphi_{\text{sca}}) \leq \pi$, the "−" sign should be used. Furthermore, one should take limits when the denominator of Eqs. (13) and (14) vanishes.
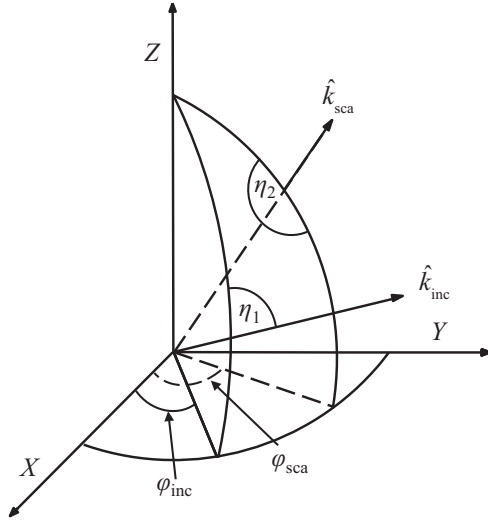
Fig. 2. The geometry of anisotropic scattering: incident $\widehat{k}_{\text{inc}}$ and scattering $\widehat{k}_{\text{sca}}$ directions. η_1 and η_2 are the rotation angles, and φ_{inc} and φ_{sca} are the azimuth angles of the incident and scattering directions, respectively.

For polarization problems, the transformation phase matrix and not just the scattering phase function describes the scattering behavior. However, the phase function is used to obtain the scattering angle Θ and a randomly chosen angle (between 0 and 2π) is utilized to derive the scattering azimuth angle. The following correction is applied:

$$\overrightarrow{\mathbf{S}}_{\text{sca}} = P_{11}^{-1} \cdot \mathbf{Z} \cdot \overrightarrow{\mathbf{S}}_{\text{inc}}. \tag{17}$$

Whenever a scattering event takes place, Θ is sampled from the phase function, replacing the transformation phase matrix $\mathbf{Z}$ with the reduced matrix $P_{11}^{-1} \cdot \mathbf{Z}$. This approach is called importance sampling method [14,41,23].

SPARTA considers either Lambertian (isotropic) or ocean surface as outlined [44]. Lambertian reflection represents a surface, which reflects isotropically and completely depolarizes the incident radiation. The angular distribution of the reflected radiation is uniform and independent of the incident direction and state of polarization. Considering a surface albedo of a_{L}, the corresponding reflection matrix is given by:

$$\mathbf{r} = \begin{pmatrix} a_{\text{L}} & 0 & 0 & 0 \\ 0 & 0 & 0 & 0 \\ 0 & 0 & 0 & 0 \\ 0 & 0 & 0 & 0 \end{pmatrix}. \tag{18}$$

To consider anisotropic and polarizing ocean reflection, the code by Mishchenko and Travis [44] has been implemented into SPARTA. It calculates the reflection matrix for rough water surfaces utilizing the Fresnel formulas. Shadowing effects are also implemented into the SPARTA code [57].

In order to efficiently obtain accurate radiance calculations, the Local Estimate Method (LEM) has been applied [14,41,42]. It accounts for the probability, p, that the photon is scattered into the direction of the sensor at each

scattering process, always considering the attenuation τ along the photon path. In the vector approach, it is given by:

$$p = \mathbf{Z}(\theta_{\text{inc}}, \varphi_{\text{inc}}; \theta_{\text{det}}, \varphi_{\text{det}}) \cdot \frac{\exp(-\tau)}{\cos(\theta_{\text{det}})}, \tag{19}$$

where θ_{det} and φ_{det} are the zenith and azimuth angles of the detector (viewing direction, subscript "det") respectively. Dividing by $\cos(\theta_{\text{det}})$ accounts for the slant area in the radiance definition.

3. Validation

SPARTA has been tested by comparison to benchmark results, involving randomly oriented prolate spheroids [58], as well as Rayleigh atmospheres and aerosol layers [34]) with a black non-scattering surface [3]. In addition, SPARTA has been validated within the model intercomparison project that the polarization working group of the International Radiation Commission (IRC) launched [22]. The performance of SPARTA in this intercomparison was excellent, considering the noise of the Monte Carlo technique in radiance calculations. The results were obtained by individual Monte Carlo simulations. Therefore, in this study, the performance of SPARTA is additionally tested against exact results from numerical solutions of the vector radiative transfer equation [46] and the tabulated values from de Haan et al. [24]. In this way, the accuracy of the model was quantified. Furthermore, its ability to correctly describe effects due to isotropic surface reflection was checked.

For molecular scattering SPARTA was validated against data from Natraj et al. [46]. This data has been computed utilizing a more sufficient approach to the representation of the X and Y functions introduced in Chandrasekhar [13] and Coulson et al. [15]. The values of the Stokes vector involve a set of different optical thicknesses (0.02–1), surface albedos (0–0.8), solar zenith angles θ_0 and viewing zenith angles θ_{det} (0–88.85°), and relative azimuth angles (azimuth angle between sun direction and viewing direction), $\phi = \varphi_{\text{det}} - \varphi_0$ (0–180°). In this work, the solar azimuth angle is set to zero and, therefore, $\phi = \varphi_{\text{det}}$.

Four test cases were defined with special emphasis on surface reflection, starting from an optically thin atmosphere ($\tau = 0.02$) to thicker cases ($\tau = 1$). A concise description of the test cases is given in Table 1, where $\mu_0 = \cos\theta_0$ is the cosine of the solar zenith angle, $\mu_{\text{det}} = \cos\theta_{\text{det}}$ is the cosine of the zenith angle of the detector, ϕ is the relative azimuth angle, α_{L} is the surface albedo, and TOA and BOA refer to the output altitudes, top of the atmosphere and bottom of the atmosphere, respectively.

Simulations were conducted for homogeneous, plane-parallel, Rayleigh layers; molecular absorption was not considered. The Rayleigh scattering phase matrix is given without the depolarization factor and is shown in Fig. 3. The number of photons used for all test cases in the validation was 10^8.

In Fig. 4 results for Case 1 are presented, which is a test for appropriate surface reflection. The three left panels

correspond to the normalized Stokes vector for the diffuse upward radiation at the TOA. The three right panels depict the relative differences in percent of SPARTA results for the Stokes vector as related to the benchmark results. Note that the fourth Stokes parameter is zero for molecular scattering, and it disappears at relative azimuth angles of 0° and 180°. The absolute value of the relative differences is less than 0.045% for I, and up to 0.076% for Q and U. The comparison for the Case 1 confirms that the Lambertian surface has been implemented correctly.

The results for the test Cases 2–4 are illustrated in Figs. 5–10. They compare the Stokes parameters for the diffuse radiation for both the BOA and the TOA for two solar zenithal angles (0° and 36.87°), and two RRA (0° and 90°) in the principle plane. The relative differences are less

than $\pm 0.15\%$ for I and less than $\pm 0.18\%$ and $\pm 0.05\%$ for Q and U for all test cases.

de Haan et al. [24] report benchmark results using the adding and doubling approach, where a set of two scattering problems has been investigated. The first scattering case considers a homogeneous plane-parallel atmosphere with a layer of water-haze droplets, optical thickness of 1, above a black surface. They selected the haze droplets introduced in Deirmendjian [18], whose scattering phase matrix expansion coefficients have been provided by de Rooij and van der Stap [17], also used by Brown and Xie [7]. The second case includes an inhomogeneous atmosphere with an optical thickness of 0.6, which is composed of two homogeneous layers and a Lambertian surface albedo of 0.1. The upper layer consists of only molecules (no absorption) with an optical thickness of 0.1. The lower one consists of a mixture of haze droplets and molecules with an optical thickness of 0.4 and 0.1 respectively.

To consider Rayleigh scattering, the full scattering phase matrix representation has been used, see Eq. (20) and Hansen and Travis [25], Emde et al. [23], whereby a depolarization factor (δ) of 0.0279 was selected, that corresponds to air molecules [13]. The scattering phase matrix elements for both particles are shown in Fig. 3.

Table 1
Test cases for comparison between SPARTA and the tabulated values by Natraj et al. [46] for pure molecular scattering. Where τ is the optical thickness, μ_0 is the cosine of the solar zenith angle, μ_{det} is the cosine of the zenithal angle of the detector, ϕ is the relative azimuth angle, α_L is the surface albedo, and TOA and BOA refer to the output altitudes, top of the atmosphere and bottom of the atmosphere, respectively.

Case	τ	μ_0	μ_{det}	ϕ	α_L	Altitude
1	0.02	0.92	0.4	Almucantar	0.00, 0.25, 0.80	TOA
2	0.10	0.80	Principle	90	0.00, 0.25, 0.80	TOA, BOA
3	0.50	0.80	Principle	90	0.00, 0.25, 0.80	TOA, BOA
4	1.00	1.00	Principle	0	0.00, 0.25, 0.80	TOA, BOA

$$\mathbf{P}(\Theta) = \frac{3}{3+\Delta} \begin{pmatrix} 1+\Delta \cdot \cos^2 \Theta & -\Delta \cdot \sin^2 \Theta & 0 & 0 \\ -\Delta \cdot \sin^2 \Theta & \Delta \cdot (1+\cos^2 \Theta) & 0 & 0 \\ 0 & 0 & 2\Delta \cdot \cos \Theta & 0 \\ 0 & 0 & 0 & (3\Delta-1) \cdot \cos \Theta \end{pmatrix},$$
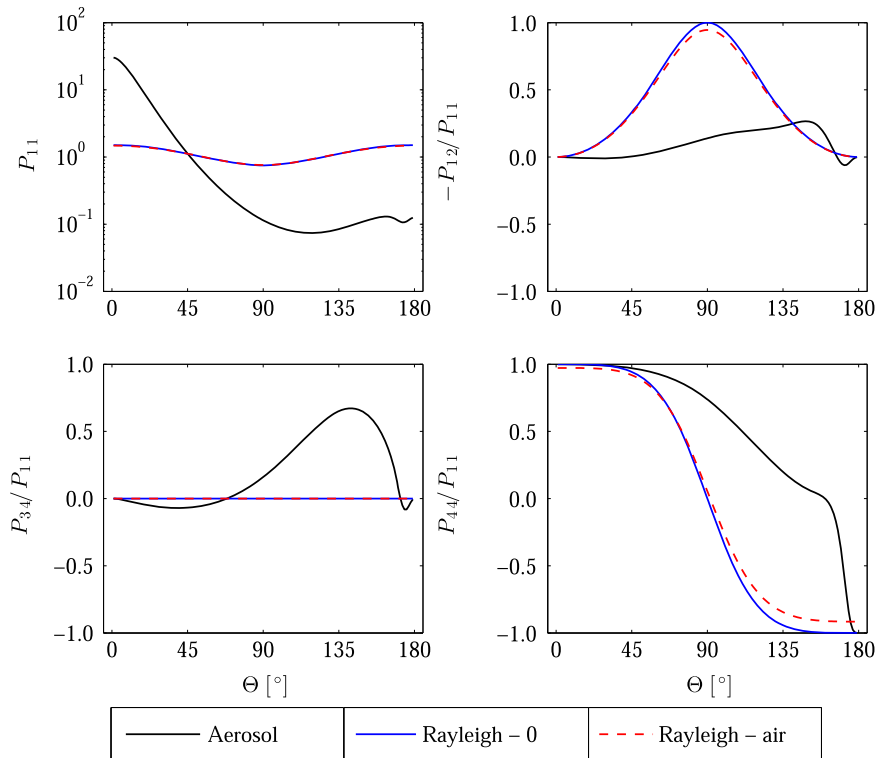

Fig. 3. Scattering phase matrix elements for the aerosol and two different molecular scattering cases. For the first Rayleigh scattering case, the depolarization factor was set to zero and for the second, the number 0.0279 was adopted, which represents air.
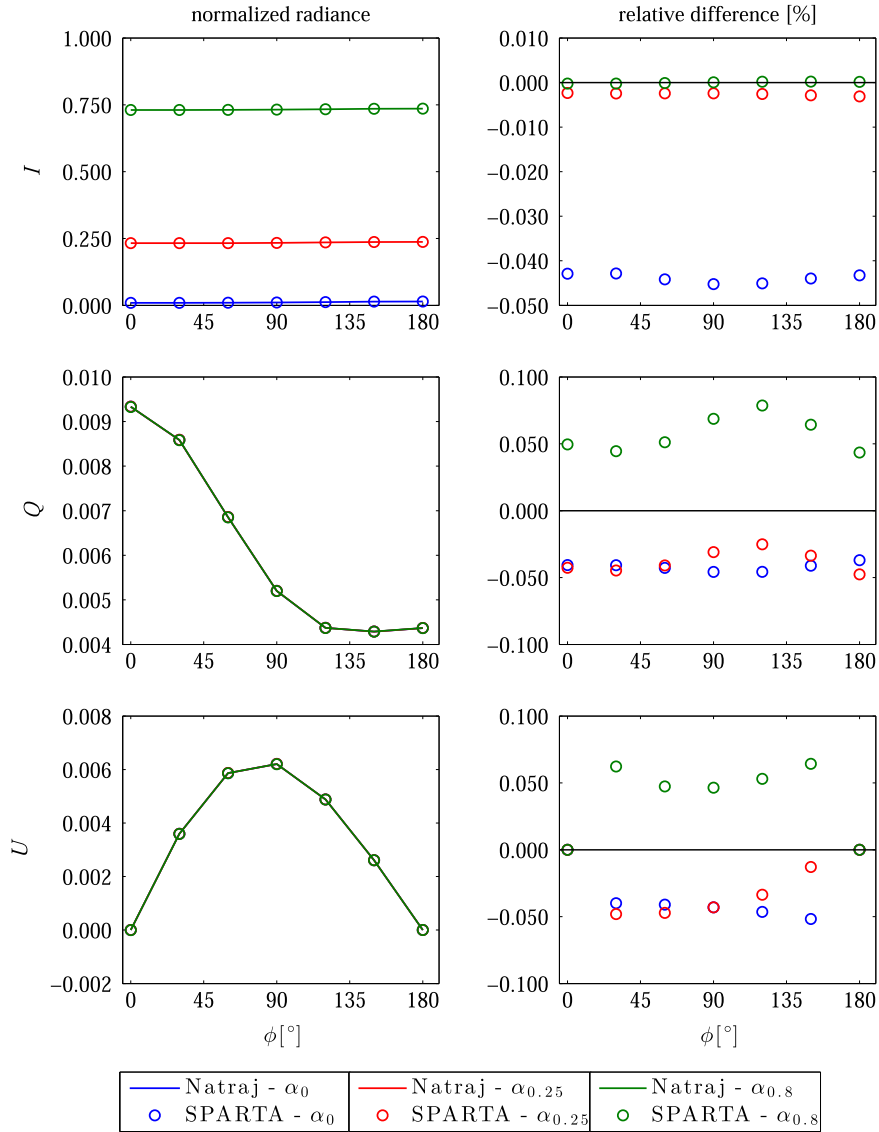
Fig. 4. Comparison between SPARTA and the tabulated values by Natraj et al. [46] for Case 1, test for surface reflection. Optically thin atmosphere ($\tau = 0.02$), $\mu_0 = 0.92$, and $\phi = 90°$. Left: normalized Stokes vector at the TOA (line – Natraj, circles – SPARTA). Right: relative differences in percent of SPARTA as correlated to the benchmark results.

where

$$\Delta = \frac{1-\delta}{1+\delta}.$$ (20)

The comparison between the tabulated values by de Haan et al. [24] and those calculated by SPARTA are compiled in Tables 2–5. They show the Stokes parameters for the reflected diffuse radiation at the TOA. The errors correspond to two standard deviations (2σ), resulting from 10 individual simulations.

The relative differences of SPARTA for all the components of the Stokes vector as compared to the tabulated values have been also computed. Values of the Stokes components close to zero are left out as they can artificially lead to large relative difference. For the homogeneous case, the absolute relative differences are less than 0.096% for the first Stokes element, less than 0.39% for Q, and up to 0.45% for U. The absolute relative differences for the inhomogeneous scattering case are less than 0.056% for the first Stokes element, 0.64% for the second Stokes element, and 0.008% for the third element. For V, the absolute values of the relative differences for both the homogeneous and inhomogeneous scattering are 2.71% and 1.55% respectively (values below 0.00005 were ignored). This is due to the fact that in the Monte Carlo method results are always subject to statistical uncertainty. The smaller the value of the Stokes vector, the larger the notable Monte Carlo noise. In order to ameliorate such noise and precisely determine V, more than 10^{10} photons should be used for the simulations (increasing computation time) or variance reduction techniques should be implemented (truncation techniques, [51,8]). Variance
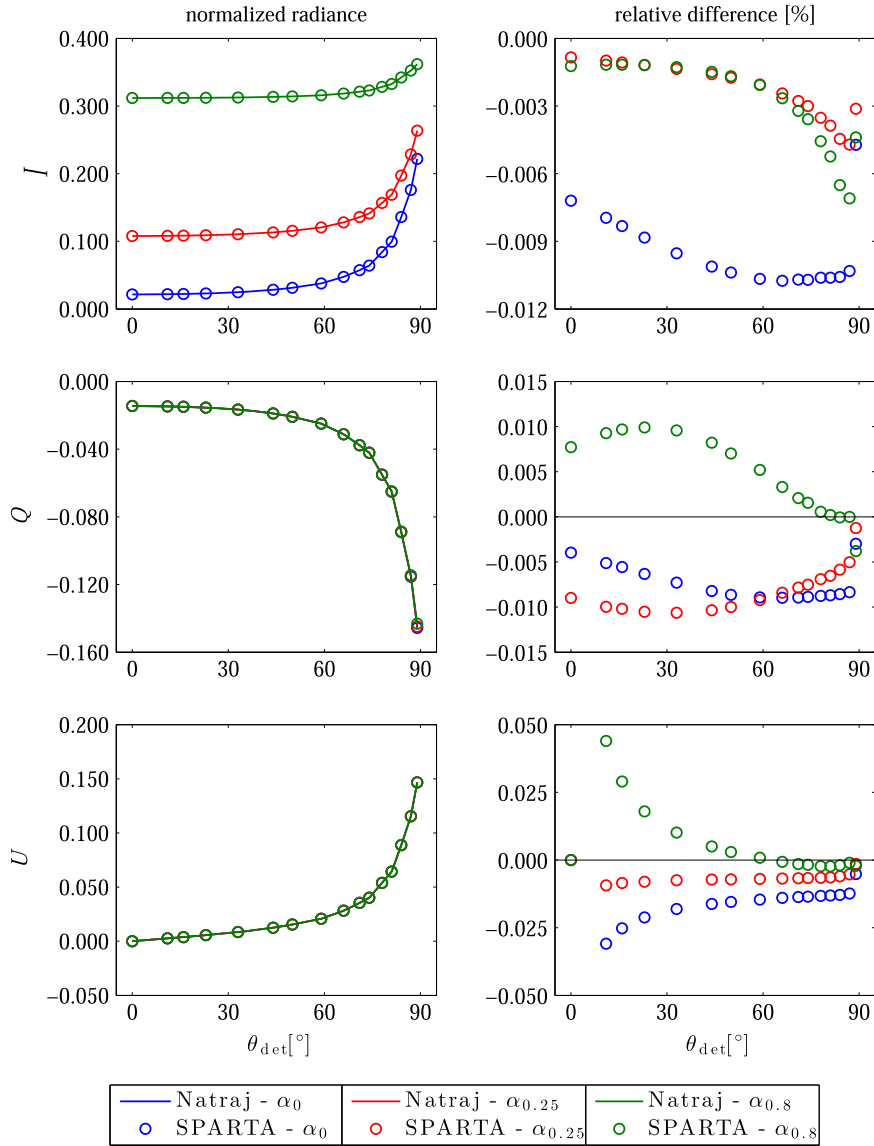
Fig. 5. Comparison between SPARTA and the tabulated values by Natraj et al. [46] for Case 2, for $\tau = 0.1$, $\mu_0 = 0.8$, and $\phi = 90°$. Left: normalized Stokes vector at the TOA (line – Natraj, circles – SPARTA). Right: relative differences in percent of SPARTA as correlated to the benchmark results.

reduction techniques may speed up simulations; however, they are not based on physics.

The comparisons demonstrated that SPARTA can handle multiple scattering and surface reflection with high accuracy and is capable of calculating polarization radiances for different atmospheric conditions.

4. Application of SPARTA

Solar radiative transfer simulations for lidar-measured fields of optical properties of Saharan dust have been performed in order to quantify the effects induced by neglecting the inhomogeneity effect in radiance and polarization simulations. Polarization radiance fields in 2D

and 1D inhomogeneous Saharan dust plumes have been calculated at 532 nm wavelength.

4.1. Measurement cases

Two case studies have been investigated. Case 1 is related to the measurements in the night from 3 to 4 June 2008, during the second phase of the SAharan Mineral dUst experiMent (SAMUM) [2,55]. The SAMUM project was divided into two sub-experiments, namely SAMUM-1 (Morocco, 2006) and SAMUM-2 (Cape Verde, 2008). The aim of the SAMUM-1 was the investigation of the microphysical, chemical, optical, and radiative properties of the mineral dust particles in the area close to the major Saharan source region [26]. SAMUM-2 focused on the characterization of Saharan dust after substantial long-
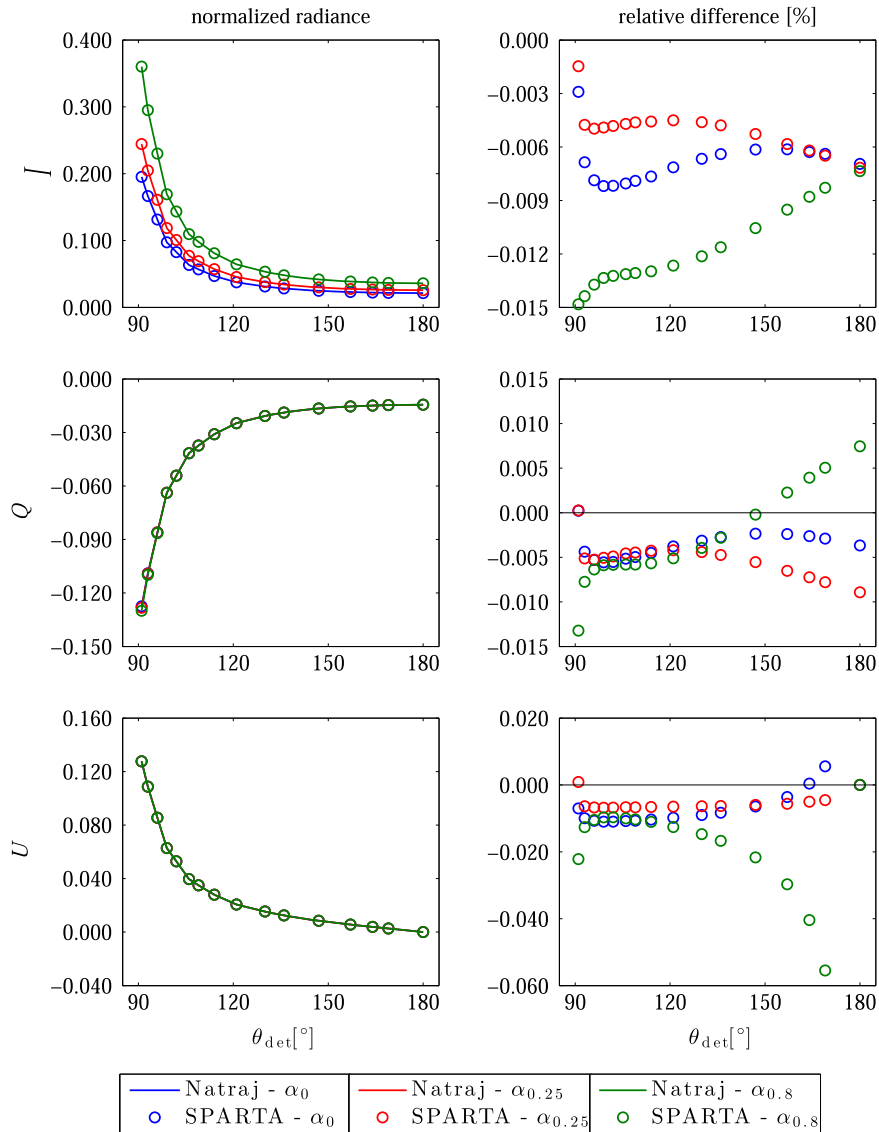
Fig. 6. Comparison between SPARTA and the tabulated values by Natraj et al. [46] for Case 2, but for the normalized Stokes vector at the BOA.

range transport [2]. Case 2 considered the nighttime measurements of 23 May 2013, from the 1-month (April–May 2013) trans-Atlantic cruise (from the Caribbean to the west coast of Africa) of the research vessel METEOR [32]. The focus of this field experiment is to determine the Saharan Air Layer along its major transport route [49,32].

The lidar measurements of extinction coefficients at 532 nm wavelength for the two measurement cases are illustrated in Figs. 11 and 12. They correspond to the height-time lidar profile in terms of the 5 and 2.3 min averaged extinction coefficient in inverse Megameters (Mm^{-1}). The observations on 3–4 June 2008 record two distinct dust layers as outlined by Tesche et al. [55]. A thin dust layer between 1 and 2 km and an elevated thicker layer between 3 and 5 km separated by a transition layer (close to clean air, but not particle-free). The lidar measurements also indicate a pure Rayleigh atmosphere above 5 km and a marine boundary layer (MBL) that is lifted to

about 1 km height. On 23 May 2013 the measured data indicate a well defined dust plume that stretched from 0.7 to 4.8 km height with maximum extinction coefficients of 340 Mm^{-1}. A MBL and a layer consisting of molecules only are documented below and above the dust layer. Further information about the later test case can be found in Kanitz et al. [32].

4.2. Molecular and aerosol scattering properties

The 2D fields of extinction and scattering coefficients, single scattering albedo and scattering phase matrix of the inhomogeneous Saharan dust were constructed on the basis of the lidar measurements sharing the geometrical and optical properties of dust plumes. The height-time lidar aerosol extinction profiles (including molecular extinction) were converted into vertically integrated optical thickness (see Fig. 13). The model domains were
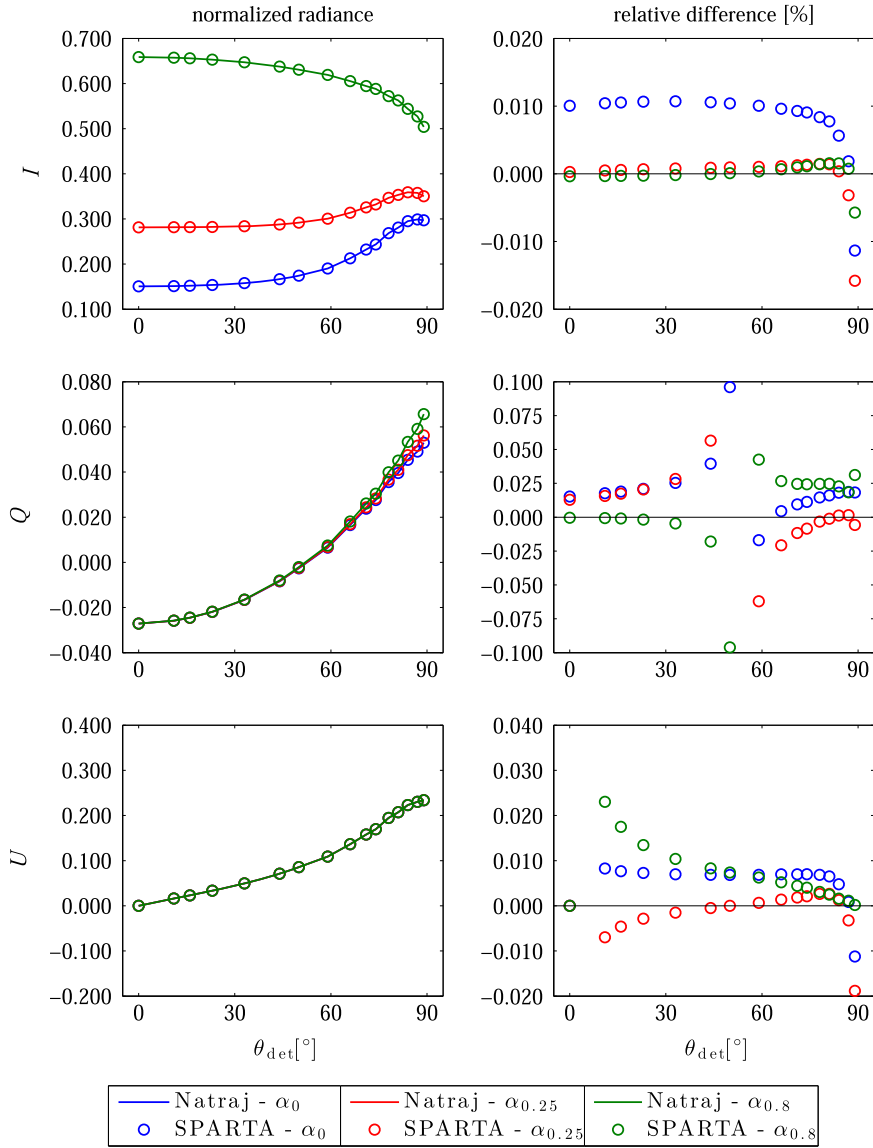
Fig. 7. Comparison between SPARTA and the tabulated values by Natraj et al. [46] for Case 3, for $\tau = 0.5$, $\mu_0 = 0.8$, and $\phi = 90°$. Left: normalized Stokes vector at the TOA (line – Natraj, circles – SPARTA). Right: relative differences in percent of SPARTA as correlated to the benchmark results.

defined by $209 \times 1 \times 168$ pixels with a size of 0.96 km along the horizontal axis (overall ~ 201.2 km), for the SAMUM measurement case, and $70 \times 1 \times 1321$ pixels with a size of 2.06 km along the horizontal axis (overall ~ 144.6 km), for the METEOR measurement case. The vertical length of the entire grid is about 10 km for both scenarios, with a pixel size of 60 m and 7.5 m, respectively.

The Rayleigh scattering phase matrix was taken in the analytical form (see Eq. (20)). The wavelength dependent depolarization factor ($\delta = 0.0842$ for $\lambda = 532$ nm) and the scattering coefficients were computed using the formulation given in Bodhaine et al. [5]. Molecular absorption was parameterized with the LOWTRAN band model [48], as adopted from the SBDART code [50]. For both scattering and absorption coefficients a tropical model atmosphere has been considered [1]. The aerosol microphysical

properties of the MBL correlate with water soluble particles for different relative humidity at 532 nm, according to the sounding measurements (OPAC database, [27,23]).

For the dust scattering properties, the scattering phase matrix data by Torge et al. [56] were used. This study draws on research conducted on the measurements in the course of the SAMUM project [31,47,30]. The optical properties of dust particles have been calculated utilizing the MIESCHKA code [59], which is a T-matrix code, for rather small spheroids with a size parameter of up to 40. For larger irregular shaped particles (size parameter of up to 143), a ray-tracing code [39] anchored in the geometric optics method has been employed. Five particle sizes have been considered with an effective radius ranging from 0.166 μm to 13.804 μm. A detailed explanation of the methods used to model the
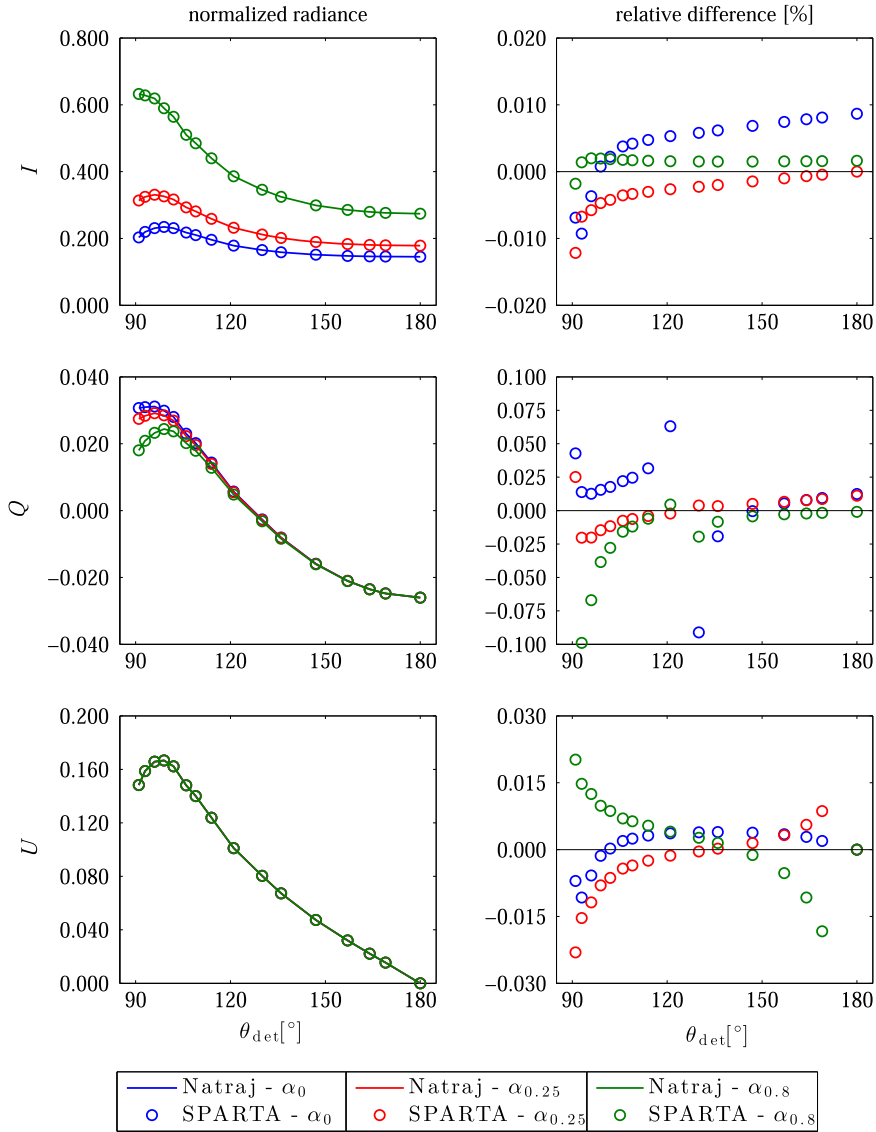
Fig. 8. Comparison between SPARTA and the tabulated values by Natraj et al. [46] for Case 3, but for the normalized Stokes vector at the BOA.

scattering phase matrices of the mineral dust particles (Fig. 14) is given in Torge et al. [56].

Fig. 14 illustrates the scattering phase matrix elements for the five particle sizes and the mean scattering phase matrix over all the sizes examined in this study.

The total scattering phase matrix $\mathbf{P}^{tot}(\Theta)$ at each grid box is derived by averaging the Rayleigh scattering phase matrix, $\mathbf{P}_r(\Theta)$, and the scattering phase matrix of dust particles, $\mathbf{P}_d(\Theta)$, weighted over their characteristic volumetric scattering coefficients (β_{sca}^r and β_{sca}^d for the individual grid box):

$$\mathbf{P}^{tot}(\Theta) = \frac{\beta_{sca}^r \cdot \mathbf{P}_r(\Theta) + \beta_{sca}^d \cdot \mathbf{P}_d(\Theta)}{\beta_{sca}^r + \beta_{sca}^d}, \tag{21}$$

Likewise, the total single scattering albedo is given by the sum of the Rayleigh scattering coefficient and the

scattering coefficient of the aerosol particles divided by the total volumetric extinction coefficient.

4.3. Monte Carlo simulations

Polarized radiative transfer simulations using SPARTA were conducted for three different solar zenith angles ($0°$, $47°$, and $70°$), the same viewing directions, and a relative azimuth angle of $0°$ above a Lambertian surface with albedo $\alpha_L = 0.05$, that corresponds to an ocean surface. Besides, the number of photons was 10^9 so that the Monte Carlo noise, resulting from the strongly peaked dust scattering phase matrices (Fig. 14), is reduced.

The 2D normalized reflectance field was compared pixel by pixel with the 1D to quantify the differences to the domain average. Results for both case studies are presented for the viewing zenith angle of $47°$, where the observed
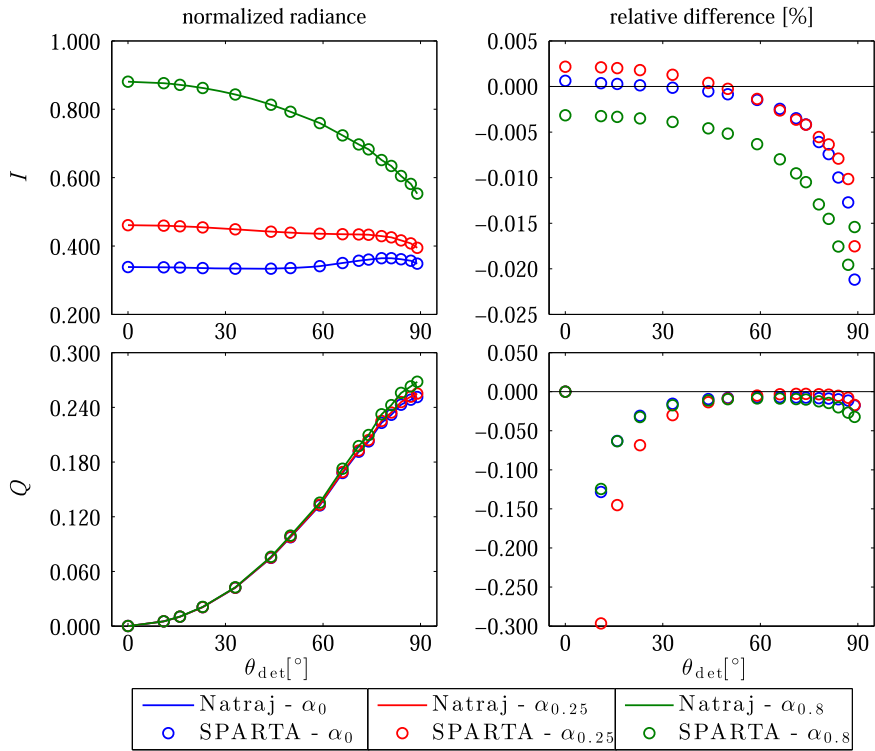
Fig. 9. Comparison between SPARTA and the tabulated values by Natraj et al. [46] for Case 4, for $\tau = 0.5$, $\mu_0 = 1$, and $\phi = 0°$. Left: normalized Stokes vector at the TOA (line – Natraj, circles – SPARTA). Right: Relative differences in percent of SPARTA as correlated to the benchmark results.
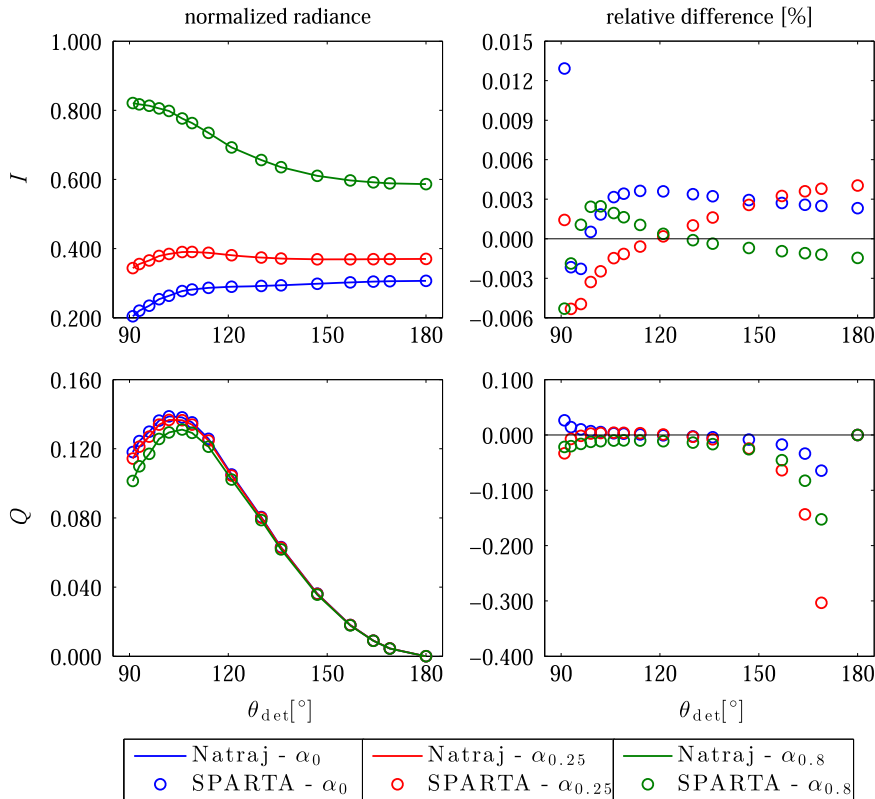

Fig. 10. Comparison between SPARTA and the tabulated values by Natraj et al. [46] for Case 4, but for the normalized Stokes vector at the BOA.

Table 2

Comparison between SPARTA and the benchmark results by de Haan et al. [24]. Stokes vector for a homogeneous layer of water-haze droplets in the reflected diffuse radiation at the TOA. The cosine of the solar zenith angle is 0.5 and the cosines of the three viewing directions are μ_{det}=0.1, 0.5, 1.0. The viewing zenith angles φ_{det} are 0° and 30°. No ground reflection. The errors correspond to two standard deviations (2σ).

μ_0=0.5	μ_{det} = 0.1		μ_{det} = 0.5		μ_{det} = 1.0	
	de Haan	SPARTA	de Haan	SPARTA	de Haan	SPARTA
φ_{det} = 0°						
I	1.10269	1.10331 ± 0.00070	0.31943	0.31953 ± 0.00010	0.03303	0.03303 ± 0.00003
Q	0.00460	0.00461 ± 0.00001	−0.00288	−0.00288 ± 0.00000	−0.00298	−0.00298 ± 0.00000
U	0.00000	0.00000 ± 0.00001	0.00000	0.00000 ± 0.00000	0.00000	0.00000 ± 0.00000
V	0.00000	0.00000 ± 0.00000	0.00000	0.00000 ± 0.00000	0.00000	0.00000 ± 0.00000
φ_{det} = 30°						
I	0.66414	0.66438 ± 0.00067	0.25209	0.25215 ± 0.00019	0.03303	0.03304 ± 0.00003
Q	0.00030	0.00030 ± 0.00001	−0.00144	−0.00144 ± 0.00000	−0.00149	−0.00149 ± 0.00000
U	−0.00277	−0.00276 ± 0.00002	−0.00414	−0.00414 ± 0.00001	−0.00258	−0.00258 ± 0.00000
V	0.00004	0.00004 ± 0.00000	0.00002	0.00002 ± 0.00000	0.00000	0.00000 ± 0.00000

Table 3

As in Table 2 but the cosine of the solar zenith angle is 0.1.

μ_0=0.1	μ_{det} = 0.1		μ_{det} = 0.5		μ_{det} = 1.0	
	de Haan	SPARTA	de Haan	SPARTA	de Haan	SPARTA
φ_{det} = 0°						
I	2.93214	2.93314 ± 0.00057	0.22054	0.22075 ± 0.00005	0.00929	0.00929 ± 0.00000
Q	0.00990	0.00987 ± 0.00000	0.00098	0.00098 ± 0.00000	−0.00082	−0.00082 ± 0.00000
U	0.00000	0.00000 ± 0.00000	0.00000	0.00000 ± 0.00000	0.00000	0.00000 ± 0.00000
V	0.00000	0.00000 ± 0.00000	0.00000	0.00000 ± 0.00000	0.00000	0.00000 ± 0.00000
φ_{det} = 30°						
I	0.76910	0.76969 ± 0.00015	0.13283	0.13293 ± 0.00003	0.00929	0.00929 ± 0.00001
Q	−0.00376	−0.00376 ± 0.00001	0.00022	0.00022 ± 0.00000	−0.00041	−0.00041 ± 0.00000
U	0.00314	0.00313 ± 0.00000	−0.00053	−0.00052 ± 0.00000	−0.00071	−0.00071 ± 0.00000
V	0.00001	0.00001 ± 0.00000	0.00001	0.00001 ± 0.00000	0.00000	0.00000 ± 0.00000

Table 4

Comparison between SPARTA and the benchmark results by de Haan et al. [24]. Stokes vector for an inhomogeneous atmosphere of molecules and water-haze droplets in the reflected diffuse radiation at the TOA above a Lambertian surface with an albedo of 0.1. The cosine of the solar zenith angle is 0.5 and the cosines of the three viewing directions are μ_{det}=0.1, 0.5, 1.0. The viewing zenith angles φ_{det} are 0 ° and 30 °. The errors correspond to two standard deviations (2σ).

| μ_0=0.5	μ_{det} = 0.1		μ_{det} = 0.5		μ_{det} = 1.0	
	de Haan	SPARTA	de Haan	SPARTA	de Haan	SPARTA
φ_{det} = 0°						
I	0.53295	0.53321 ± 0.00017	0.20843	0.20851 ± 0.00006	0.09368	0.09370 ± 0.00003
Q	−0.02834	−0.02835 ± 0.00004	−0.03630	−0.03630 ± 0.00002	−0.02416	−0.02416 ± 0.00001
U	0.00000	0.00001 ± 0.00004	0.00000	0.00000 ± 0.00001	0.00000	0.00000 ± 0.00000
V	0.00000	0.00000 ± 0.00000	0.00000	0.00000 ± 0.00000	0.00000	0.00000 ± 0.00000
φ_{det} = 30°						
I	0.41814	0.41823 ± 0.00016	0.18497	0.18501 ± 0.00007	0.09368	0.09369 ± 0.00002
Q	−0.00006	−0.00006 ± 0.00004	−0.01965	−0.01965 ± 0.00002	−0.01208	−0.01208 ± 0.00001
U	−0.07311	−0.07311 ± 0.00004	−0.04140	−0.04140 ± 0.00002	−0.02092	−0.02092 ± 0.00001
V	0.00011	0.00011 ± 0.00000	0.00004	0.00004 ± 0.00000	0.00000	0.00000 ± 0.00000

effects are largest. Figs. 15 and 16 illustrate the relative differences (RD) in percent between the 2D mode (horizontal + vertical photon transport) and the 1D mode (only vertical photon transport), for the different sun positions as a function of the pixel number. The upper plots depict the first Stokes component (I) and the lower plots the second component (Q).

In Fig. 15, SAMUM case, the domain-averaged reflectivity is almost identical for both the 1D and 2D calculations. However, at the regions with large spatial gradient in optical thickness, the radiance field of the 2D mode differs by about ± 12.2% for I and ± 8.1% for Q from the field of the 1D mode. Note that the use of periodic boundary conditions employed in SPARTA may provide an artificial strong
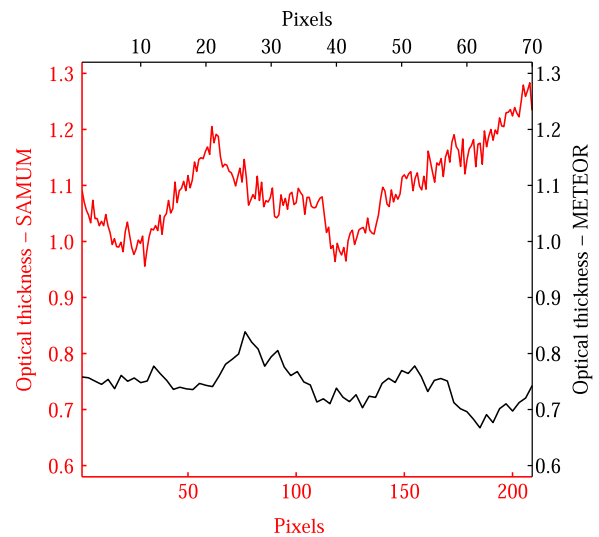
Table 5
As in Table 4 but the cosine of the solar zenith angle is 0.1.

$\mu_0 = 0.1$	$\mu_{det} = 0.1$		$\mu_{det} = 0.5$		$\mu_{det} = 1.0$	
	de Haan	SPARTA	de Haan	SPARTA	de Haan	SPARTA
$\varphi_{det} = 0°$						
I	0.52277	0.52297 ± 0.00007	0.10659	0.10665 ± 0.00002	0.02601	0.02601 ± 0.00000
Q	0.01151	0.01150 ± 0.00002	-0.00519	-0.00519 ± 0.00001	-0.01498	-0.01498 ± 0.00000
U	0.00000	0.00000 ± 0.00001	0.00000	0.00000 ± 0.00000	0.00000	0.00000 ± 0.00000
V	0.00000	0.00000 ± 0.00000	0.00000	0.00000 ± 0.00000	0.00000	0.00000 ± 0.00000
$\varphi_{det} = 30°$						
I	0.27630	0.27639 ± 0.00006	0.08363	0.08366 ± 0.00002	0.02601	0.02601 ± 0.00001
Q	0.03437	0.03438 ± 0.00002	0.00384	0.00384 ± 0.00001	-0.00749	-0.00749 ± 0.00000
U	-0.01604	-0.01605 ± 0.00001	-0.01449	-0.01449 ± 0.00001	-0.01298	-0.01298 ± 0.00000
V	0.00003	0.00003 ± 0.00000	0.00002	0.00002 ± 0.00000	0.00000	0.00000 ± 0.00000
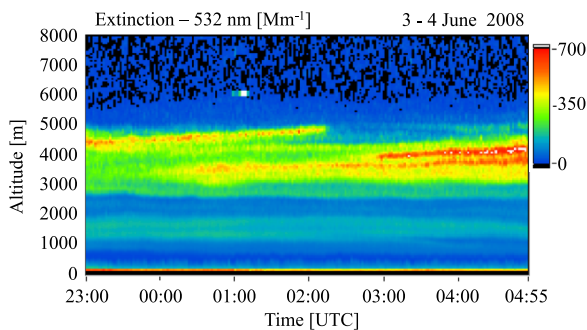
Fig. 11. Height–time display of lidar measurements during the SAMUM-2 field experiment in terms of the 2.3 min-averaged extinction coefficient. Measurement example: Cape Verde, 3–4 June 2008.
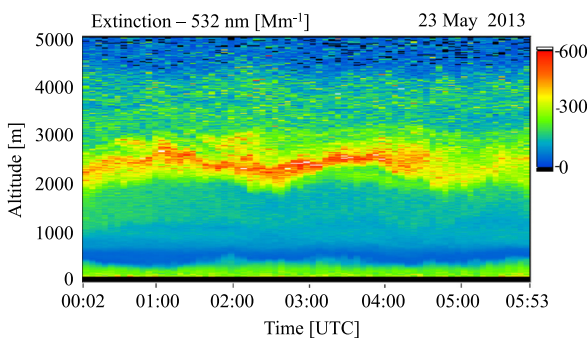
Fig. 12. Height–time display of lidar measurements during the METEOR cruise in terms of the 5 min-averaged extinction coefficient. Measurement example: Cape Verde, 23 May 2013.

Fig. 13. Optical thickness at 532 nm for the SAMUM (red line) and METEOR (black line) measurement cases. (For interpretation of the references to color in this figure caption, the reader is referred to the web version of this paper.)

variability that is resolved by the larger horizontal pixel size, and more importantly, by the lower gradient in optical thickness (see Fig. 13).

The RD values and the locations of maxima and minima follow the pattern of the optical thickness for both measurement cases (Fig. 13).

These results are in line with those of Scheirer and Macke [52], Benner and Evans [4], Di Giuseppe and Tompkins [20], Cahalan et al. [9], and Torge et al. [56]. These authors concluded that the radiative effects due to the neglect of the inhomogeneity effect are dominant in areas with strong horizontal gradient in optical thickness.

5. Summary and conclusions

SPARTA (Solver for Polarized Atmospheric Radiative Transfer Applications), a new 3D vector radiative transfer model, has been introduced. SPARTA utilizes the statistical forward Monte Carlo method for efficient column-response pixel-based radiance calculation including
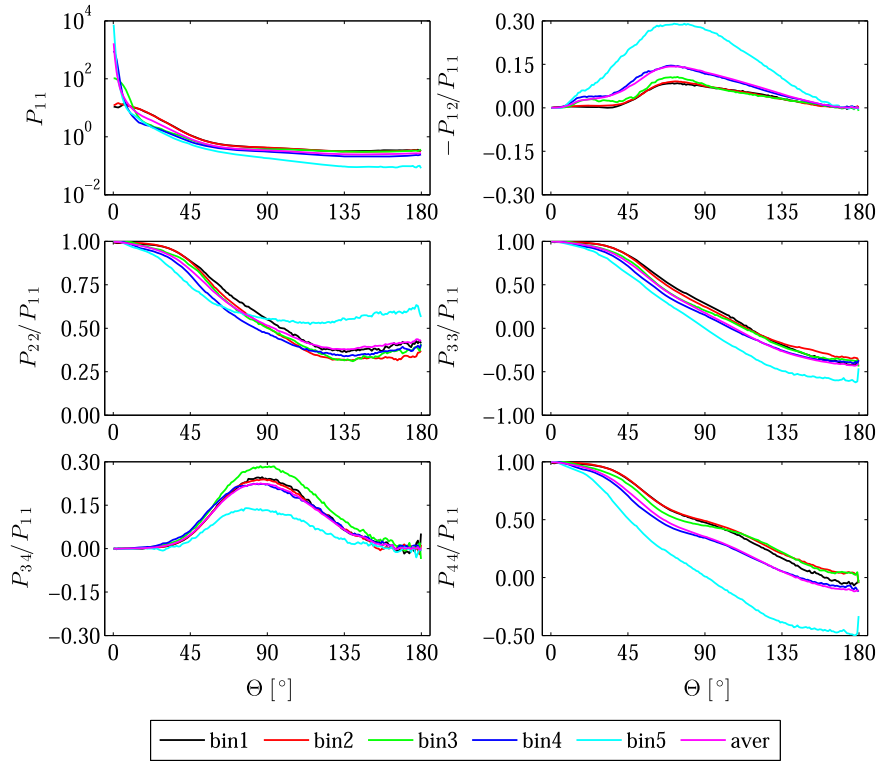
gradient, moving photons from the right region of the domain to the left, leading to the largest differences between the 1D and 2D. Increasing the solar zenith angle the RD, as well as the range of RD are increasing because the photon path length is increasing and, therefore, the number of scattering events is increasing. The radiative effects are more pronounced in I rather than in Q. In the same direction are the findings for the METEOR case (see Fig. 16) for the first Stokes component I, but the resulting RD are much lower, less than 5.1%. For Q no increase of RD with an increase of solar zenith angle was observed. RD range up to 3.1%. The smaller differences are explained by the lower

Fig. 14. Scattering phase matrix elements for the five different particle sizes and the mean scattering phase matrix elements over all the different sizes considered for this study.
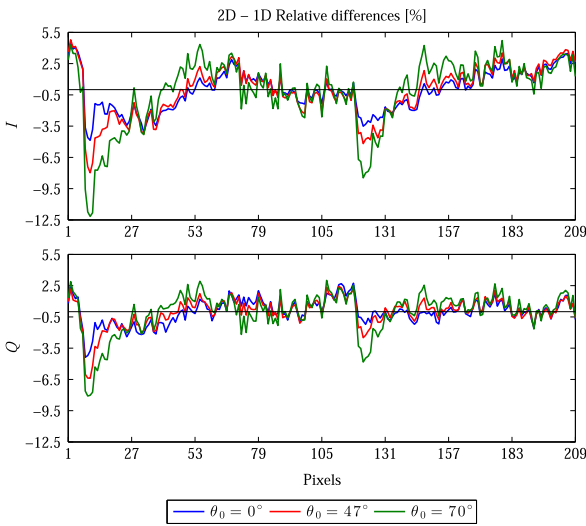

Fig. 15. SPARTA simulated reflectance field including polarization for the SAMUM case at 532 nm: relative differences in percent between the 2D mode (horizontal + vertical photon transport) and the 1D mode (only vertical photon transport) for three different solar zenith angles $0°$, $47°$, and $70°$ at a viewing zenith angle of $47°$. Upper: first Stokes element. Lower: second Stokes element.
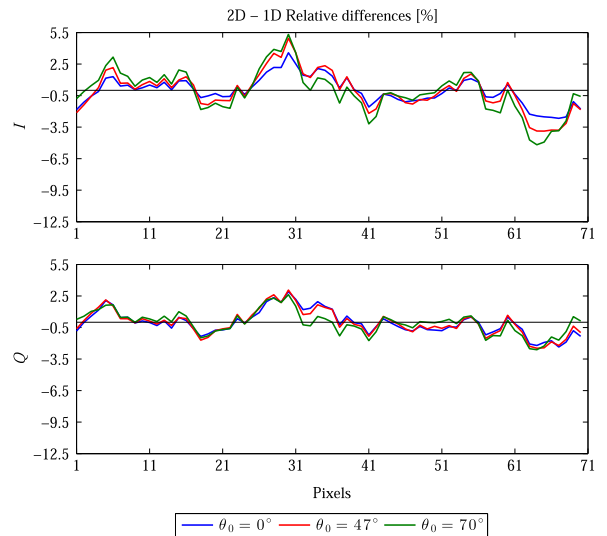
Fig. 16. The same as in Fig. 15 but for the METEOR case.

polarization effects for 3D inhomogeneous cloudless and cloudy atmospheres. SPARTA is going to be a freely available, user-friendly model. The importance sampling method implemented in the model has proven to be an

efficient approach to calculate scattering directions. In order to reduce the noise in radiance calculations for strongly peaked scattering phase matrices the Local Estimate Method has been applied.

SPARTA has been tested for black surfaces by comparison to benchmark results for different atmospheric conditions [3]. It took part in the International Radiation Commission (IRC) polarized radiative transfer model

intercomparison [22]. In this work, the accuracy of the code was tested for Lambertian surface reflection. Validations of the model output have been carried out against the tabulated values by Natraj et al. [46] and de Haan et al. [24]. Overall, the comparisons demonstrated that the performance of SPARTA is excellent. All deviations found for the last component of the Stokes vector for the highly asymmetric scattering phase matrices can be explained by the noise of the Monte Carlo technique in radiance calculations. The noisiness of the signal is a function of the number of photons. Increasing the selected number of photons could diminish the noise.

By means of SPARTA a study has been carried out to investigate the polarization radiative effects due to the neglect of dust plume inhomogeneities in radiative transfer simulations. Polarized radiance fields in 2D and 1D inhomogeneous Saharan dust fields have been calculated at 532 nm wavelength. The domain-averaged normalized radiances of reflection are insignificant between the 1D and 2D modes. However, local deviations are observed since extinction is hinge on horizontal spatial variability. In the areas with large spatial gradient in optical thickness, the radiance fields of the 2D scenario differ about $\pm 12.2\%$ for I and $\pm 8.1\%$ for Q from the fields of the 1D scenario.

In this paper, results are presented only for two lidar-based measurement cases. Future work should aim at developing correction schemes that account for observable gradients of optical thickness in the dust fields. Moreover, further research should be conducted in order to explore the polarization radiative effects in 3D realistic mineral cloud schemes.

Acknowledgments

References

[1] Anderson G, Clough S, Kneizys F, Chetwynd J, Shettle E. AFGL atmospheric constituent profiles (0–120 km). Technical Report AFGL-TR-86-0110. Hanscom AFB, MA: AFGL (OPI); 1986.

[2] Ansmann A, Petzold A, Kandler K, Tegen I, Wendisch M, Müller D, et al. Saharan mineral dust experiments SAMUM-1 and SAMUM-2: What have we learned?. Tellus B 2011;63:403–29.

[3] Barlakas V, Macke A, Wendisch M, Ehrlich A. Implementation of polarization in a 3D Monte Carlo radiative transfer model. Wissenschaftliche Mitteilungen aus dem Institut für Meteorologie der Universitt Leipzig, vol. 52, 2014. p. 1–14. iSBN: 978-3-9814401-2-6.

[4] Benner TC, Evans KF. Three-dimensional solar radiative transfer in small tropical cumulus fields derived from high-resolution imagery. J Geophys Res 2001;106:14975–84.

[5] Bodhaine BA, Wood NB, Dutton EG, Slusser JR. On Rayleigh optical depth calculations. J Atmos Ocean Technol 1999;16:1854–61.

[6] Boesche E, Stammes P, Ruhtz T, Preusker R, Fischer J. Effect of aerosol microphysical properties on polarization of skylight: sensitivity study and measurements. Appl Opt 2006;45:8790–805.

[7] Brown AJ, Xie Y. Symmetry relations revealed in Mueller matrix hemispherical maps. J Quant Spectrosc Radiat Transf 2012;113: 644–51.

[8] Buras R, Mayer B. Efficient unbiased variance reduction techniques for Monte Carlo simulations of radiative transfer in cloudy atmospheres: the solution. J Quant Spectrosc Radiat Transf 2011;112: 434–47.

[9] Cahalan RF, Oreopoulos L, Marshak A, Evans KF, Davis AB, Pincus R, et al. The i3rc: bringing together the most advanced radiative transfer tools for cloudy atmospheres. Bull Am Meteorol Soc 2005;86:1275–93.

[10] Cairns B, Russell EE, LaVeigne JD, Tennant PMW. Research scanning polarimeter and airborne usage for remote sensing of aerosols. In: Proceedings of the SPIE, vol. 5158, 2003. p. 33–44.

[11] Cairns B, Russell EE, Travis LD. Research scanning polarimeter: calibration and ground-based measurements. In: Proceedings of the SPIE, vol. 3754, 1999. p. 186–96.

[12] Cashwell ED, Everett CJ. A practical manual on the Monte Carlo method for random walk problems. New York: Pergamon; 1959.

[13] Chandrasekhar S. Radiative transfer. Dover books on intermediate and advanced mathematics. New York: Dover Publications; 1960.

[14] Collins DG, Blättner WG, Wells MB, Horak HG. Backward Monte Carlo calculations of the polarization characteristics of the radiation emerging from spherical-shell atmospheres. Appl Opt 1972;11: 2684–96.

[15] Coulson KL, Dave JV, Sekera Z. Tables related to radiation emerging from a planetary atmosphere with Rayleigh scattering. Berkeley: University of California Press; 1960.

[16] Davis A, Marshak A, Cahalan R, Wiscombe W. The landsat scale break in stratocumulus as a three-dimensional radiative transfer effect: implications for cloud remote sensing. J Atmos Sci 1997;54:241–60.

[17] de Rooij WA, van der Stap CCAH. Expansion of Mie scattering matrices in generalized spherical functions. Astron Astrophys 1984;131:237–48.

[18] Deirmendjian D. Electromagnetic scattering on spherical polydispersions. R (Rand Corporation), New York: American Elsevier Pub. Co.; 1969.

[19] Deschamps PY, Breon FM, Leroy M, Podaire A, Bricaud A, Buriez JC, et al. The polder mission: instrument characteristics and scientific objectives. IEEE Trans Geosci Remote Sens 1994;32:598–615.

[20] Di Giuseppe F, Tompkins AM. Effect of spatial organization on solar radiative transfer in three-dimensional idealized stratocumulus cloud fields. J Atmos Sci 2003;60:1774–94.

[21] Diner DJ, Xu F, Garay MJ, Martonchik JV, Rheingans BE, Geier S, et al. The airborne multiangle spectropolarimetric imager (airmspi): a new tool for aerosol and cloud remote sensing. Atmos Meas Tech Discuss 2013;6:1717–69.

[22] Emde C, Barlakas V, Cornet C, Evans F, Korkin S, Ota Y, et al. IPRT polarized radiative transfer model intercomparison project—Phase A. J Quant Spectrosc Radiat Transf 2015;164:8–36.

[23] Emde C, Buras R, Mayer B, Blumthaler M. The impact of aerosols on polarized sky radiance: model development, validation, and applications. Atmos Chem Phys 2010;10:383–96.

[24] de Haan JF, Bosma PB, Hovenier JW. The adding method for multiple scattering calculations of polarized light. Astron Astrophys 1987;183:371–91.

[25] Hansen JE, Travis LD. Light scattering in planetary atmospheres. Space Sci Rev 1974;16:527–610.

[26] Heintzenberg J. The SAMUM-1 experiment over Southern Morocco: overview and introduction. Tellus B 2009;61:2–11.

[27] Hess M, Koepke P, Schult I. Optical properties of aerosols and clouds: the software package opac. Bull Am Meteorol Soc 1998;79:831–44.

[28] van de Hulst HC. Light scattering by small particles. Dover books on physics series. Mineola, NY: Dover Publications; 1981.

[29] IPCC, Climate change 2013: the physical science basis. Cambridge, UK: Cambridge University Press; 2013.

[30] Kandler K, Lieke K, Benker N, Emmel C, Küpper M, Müller-Ebert D, et al. Electron microscopy of particles collected at Praia, Cape Verde, during the Saharan mineral dust experiment: particle chemistry, shape, mixing state and complex refractive index. Tellus B 2011;63:475–96.

[31] Kandler K, Schütz L, Deutscher C, Ebert M, Hofmann H, Jäckel S, et al. Size distribution, mass concentration, chemical and mineralogical composition and derived optical parameters of the boundary layer

aerosol at Tinfou, Morocco, during SAMUM 2006. Tellus B, 2009;61:32–50.

[32] Kanitz T, Engelmann R, Heinold B, Baars H, Skupin A, Ansmann A. Tracking the Saharan air layer with shipborne lidar across the tropical Atlantic. Geophys Res Lett 2014;41:1044–50.

[33] Kaufman YJ, Tanre D, Boucher O. A satellite view of aerosols in the climate system. Nature 2002;419:215–23.

[34] Kokhanovsky AA, Budak VP, Cornet C, Duan M, Emde C, Katsev IL, et al. Benchmark results in vector atmospheric radiative transfer. J Quant Spectrosc Radiat Transf 2010;111:1931–46.

[35] Li L, Li Z, Li K, Blarel L, Wendisch M. A method to calculate stokes parameters and angle of polarization of skylight from polarized CIMEL sun/sky radiometers. J Quant Spectrosc Radiat Transf 2014;149:334–46.

[36] Li Z, Goloub P, Dubovik O, Blarel L, Zhang W, Podvin T, et al. Improvements for ground-based remote sensing of atmospheric aerosol properties by additional polarimetric measurements. J Quant Spectrosc Radiat Transf 2009;110:1954–61.

[37] Liou KN. Influence of cirrus clouds on weather and climate processes: a global perspective. Mon Weather Rev 1986;114:1167–99.

[38] Liou KN. An introduction to atmospheric radiation. International geophysics series. Cambridge, Massachusetts: Academic Press; 2002.

[39] Macke A, Mishchenko M, Carlson B, Muinonen K. Scattering of light by large spherical, spheroidal, and circular cylindrical scatterers: geometrical optics approximation versus T-matrix method. In: Smith W, Stamnes K, editors. IRS 96: Current problems in atmospheric radiation. Hampton: A. Deepak Publ.; 1997. p. 822–5.

[40] Macke A, Mitchell DL. Bremen LV. Monte Carlo radiative transfer calculations for inhomogeneous mixed phase clouds. Phys Chem Earth 1999;24:37–241.

[41] Marchuk GI, Mikhailov GA, Nazaraliev MA. The Monte Carlo methods in atmospheric optics. Springer series in optical sciences. Berlin, Heidelberg: Springer; 1980.

[42] Marshak A, Davis A. 3D radiative transfer in cloudy atmospheres. Physics of earth and space environments. Berlin, Heidelberg: Springer; 2005. iSBN: 978-3-540-23958-1.

[43] Mishchenko, MI. Gustav Mie and the fundamental concept of electromagnetic scattering by particles: a perspective. J Quant Spectrosc Radiat Transf 2009;110:1210–1222 [XI Conference on Electromagnetic and Light Scattering by Non-Spherical Particles: 2008].

[44] Mishchenko MI, Travis LD. Satellite retrieval of aerosol properties over the ocean using polarization as well as intensity of reflected sunlight. J Geophys Res 1997;102:16989–7013.

[45] Mishchenko MI, Travis LD, Lacis AA. Scattering, absorption, and emission of light by small particles. Cambridge, UK: Cambridge University Press; 2002.

[46] Natraj V, Li KF, Yung YL. Rayleigh scattering in planetary atmospheres: corrected tables through accurate computation of X and Y functions. Astrophys J 2009;691:1909–2009.

[47] Otto S, Bierwirth E, Weinzierl B, Kandler K, Esselborn M, Tesche M, et al. Solar radiative effects of a Saharan dust plume observed during SAMUM assuming spheroidal model particles. Tellus B 2009;61:270–96.

[48] Pierluissi JH, Peng GS. New molecular transmission band models for lowtran. Opt Eng 1985;24:243541.

[49] Prospero JM, Carlson TN. Vertical and areal distribution of saharan dust over the Western equatorial north Atlantic Ocean. J Geophys Res 1972;77:5255–65.

[50] Ricchiazzi P, Yang S, Gautier C, Sowle D. Sbdart: a research and teaching software tool for plane-parallel radiative transfer in the earth's atmosphere. Bull Am Meteorol Soc 1998;79:2101–14.

[51] Rozanov VV, Lyapustin AI. Similarity of radiative transfer equation: error analysis of phase function truncation techniques. J Quant Spectrosc Radiat Transf 2010;111:1964–79.

[52] Scheirer R, Macke A. On the accuracy of the independent column approximation in calculating the downward fluxes in the uva, uvb, and par spectral ranges. J Geophys Res 2001;106:14301–12.

[53] Scheirer R, Macke A. Cloud inhomogeneity and broadband solar fluxes. J Geophys Res 2003;108:4599.

[54] Stokes GG. On the Composition and Resolution of Streams of Polarized Light from Different Sources. Proc Camb Philos Soc: Math Phys Sci. Cambridge, UK: Cambridge Philosophical Society, 1852, http://ebooks.cambridge.org/chapter.jsf?bid=CBO9780511702266&cid=CBO9780511702266A027.

[55] Tesche M, Gross S, Ansmann A, Müller D, Althausen D, Freudenthaler V, et al. Profiling of Saharan dust and biomass-burning smoke with multiwavelength polarization Raman lidar at Cape Verde. Tellus B 2011;63:649–76.

[56] Torge A, Macke A, Heinold B, Wauer J. Solar radiative transfer simulations in Saharan dust plumes: particle shapes and 3-D effect. Tellus B 2011;63:770–80.

[57] Tsang L, Kong J, Shin R. Theory of microwave remote sensing. Wiley series in remote sensing. New York: John Wiley, 1985.

[58] Wauben WMF, Hovenier JW. Polarized radiation of an atmosphere containing randomly-oriented spheroids. J Quant Spectrosc Radiat Transf 1992;47:491–504.

[59] Wauer J, Schmidt K, Rother T, Ernst T, Hess M. Two software tools for plane-wave scattering on nonspherical particles in the German Aerospace Center's virtual laboratory. Appl Opt 2004;43:6371–9.

[60] Wendisch M, Yang P. Theory of atmospheric radiative transfer. Physics textbook. Weinheim, Germany: Wiley-VCH; 2012 iSBN: 978-3-527-40836-8.